

PAPER • OPEN ACCESS

Temperature-mediated structural evolution of vapor-phase deposited cyclosiloxane polymer thin films for enhanced mechanical properties and thermal conductivity



To cite this article: Weiwei Du *et al* 2023 *Int. J. Extrem. Manuf.* **5** 025101

View the [article online](#) for updates and enhancements.

You may also like

- [Autoregressive Planet Search: Application to the *Kepler* Mission](#)
Gabriel A. Caceres, Eric D. Feigelson, G. Jogesh Babu et al.
- [Kepler Presearch Data Conditioning I—Architecture and Algorithms for Error Correction in Kepler Light Curves](#)
Martin C. Stumpe, Jeffrey C. Smith, Jeffrey E. Van Cleve et al.
- [Progress in polymer-derived functional silicon-based ceramic composites for biomedical and engineering applications](#)
A Francis

Temperature-mediated structural evolution of vapor–phase deposited cyclosiloxane polymer thin films for enhanced mechanical properties and thermal conductivity

Weiwei Du^{1,2,5}, Jing Tu^{3,5}, Mingjun Qiu^{1,2}, Shangyu Zhou^{1,2}, Yingwu Luo¹, Wee-Liat Ong^{3,4,*}  and Junjie Zhao^{1,2,*} 

¹ State Key Laboratory of Chemical Engineering, College of Chemical and Biological Engineering, Zhejiang University, 38 Zheda Rd, Hangzhou 310027, People's Republic of China

² Institute of Zhejiang University—Quzhou, 78 Jiu Hua Boulevard North, Quzhou, Zhejiang 324000, People's Republic of China

³ ZJU-UIUC Institute, College of Energy Engineering, Zhejiang University, Haining, Jiaxing, Zhejiang 314400, People's Republic of China

⁴ State Key Laboratory of Clean Energy Utilization, Zhejiang University, Hangzhou, Zhejiang 310027, People's Republic of China

E-mail: weeong@intl.zju.edu.cn and junjiezhao@zju.edu.cn

Received 1 November 2022, revised 27 December 2022

Accepted for publication 20 March 2023

Published 3 April 2023



CrossMark

Abstract

Polymer-derived ceramic (PDC) thin films are promising wear-resistant coatings for protecting metals and carbon–carbon composites from corrosion and oxidation. However, the high pyrolysis temperature hinders the applications on substrate materials with low melting points. We report a new synthesis route for PDC coatings using initiated chemical vapor deposited poly(1,3,5-trivinyl-1,3,5-trimethylcyclotrisiloxane) (pV₃D₃) as the precursor. We investigated the changes in siloxane moieties and the network topology, and proposed a three-stage mechanism for the thermal annealing process. The rise of the connectivity number for the structures obtained at increased annealing temperatures was found with strong correlation to the enhanced mechanical properties and thermal conductivity. Our PDC films obtained via annealing at 850 °C exhibit at least 14.6% higher hardness than prior reports for PDCs synthesized below 1100 °C. Furthermore, thermal conductivity up to 1.02 W (mK)^{−1} was achieved at the annealing temperature as low as 700 °C, which is on the same order of magnitude as PDCs obtained above 1100 °C. Using minimum thermal conductivity models, we found that the thermal transport is dominated by diffusons in the films below the percolation of rigidity, while ultra-short mean-free path phonons contribute to the thermal conductivity of the

⁵ These authors contributed equally.

* Authors to whom any correspondence should be addressed.



Original content from this work may be used under the terms of the [Creative Commons Attribution 4.0 licence](https://creativecommons.org/licenses/by/4.0/). Any further distribution of this work must maintain attribution to the author(s) and the title of the work, journal citation and DOI.

films above the percolation threshold. The findings of this work provide new insights for the development of wear-resistant and thermally conductive PDC thin films for durable protection coatings.

Supplementary material for this article is available [online](#)

Keywords: polymer-derived ceramics, vapor-phase deposition, mechanical properties, thermal conductivity, thin films

1. Introduction

Polymer-derived ceramics (PDCs) are fabricated through the pyrolysis of organosilicon polymer precursors. The synthesis routes for PDCs can be generally applied to ceramic fibers, coatings, and composites [1, 2]. Among these form factors, PDC thin films are of particular interest for protecting the surface of carbon materials, C/C composites and metals against corrosion and wear [3–9]. High operating temperatures and chemically harsh environments set high demands for the durability and wear resistance of PDC coatings which are closely associated with the mechanical properties of the thin film materials. In applications related to heat transfer, such as steam methane reforming reactors and heat exchangers, high thermal conductivity and small coating thickness are desired to reduce the heat transfer resistance of the protecting layers on the equipment [10].

Previous studies have explored various polymer precursors for PDCs, including polysiloxanes (e.g. polyhydromethylsiloxane [11, 12], poly(triethoxysilane-co-methyldiethoxysilane) [13], and SR 350 resin [14]) and polysilsequioxanes [15]. The amount and forms of the carbon content in the structure [16, 17] and the network connectivity [18] are generally affected by the pyrolysis conditions [13], which are important factors for the mechanical properties of PDCs. While many precursors and pyrolysis conditions have been investigated, the typical process temperature for PDCs often exceeds 1000 °C, a threshold temperature not met by many engineering materials for daily applications (e.g. austenitic Cr–Ni steels (AISI 310 and 316) below 900 °C [8]). Hence, an immediate challenge is to find proper PDC precursors that are processable at low temperatures.

In this study, we report a new synthesis route for PDC films using vapor-phase deposited poly(1,3,5-trivinyl-1,3,5-trimethylcyclotrisiloxane) (pV_3D_3) as the precursor. Although solution-based methods such as spraying [19], dip coating and spin coating [20] are often utilized to coat the polymer precursors for PDCs, these methods are difficult to apply to non-planar substrates and poor-wetting surfaces [21]. Alternatively, initiated chemical vapor deposition (iCVD) provides a one-step, solvent free approach to deposit conformal polymer films with thickness control at nanometer scale [22, 23]. This dry process avoids dewetting and pinhole defects that may appear in solution-based methods, and allows grafting to increase the adhesion to the substrate [24]. Polycyclosiloxane thin films synthesized via iCVD have been reported with low dielectric constants, low surface energy,

and biocompatible properties, which are promising insulating layers [25, 26] and antifouling coatings [27, 28]. While thermal treatments to iCVD poly(1,3,5,7-tetravinyl-1,3,5,7-tetramethylcyclotetrasiloxane) (pV_4D_4) films for low-k dielectrics [29] and separation membranes [30] have been previously reported, how temperature-mediated structural changes affect the mechanical properties and thermal conductivity of the PDC films derived from iCVD polycyclosiloxane templates have not yet been investigated as far as we know.

We investigated the structural evolution of iCVD pV_3D_3 films after thermal annealing at various temperatures, and explored the relationship between the structure and the mechanical/thermal properties. Fourier transform infrared spectroscopy (FTIR), X-ray photoelectron spectroscopy (XPS) and X-ray reflectivity (XRR) were conducted to determine the changes in structures after annealing. Furthermore, the thermal transport in these annealed pV_3D_3 films was measured using the frequency domain thermoreflectance (FDTR), and elucidated using thermal conductivity models for amorphous materials. The results reported here are expected to pave the way for PDC coatings on substrates with low melting points.

2. Methods

2.1. Synthesis and thermal annealing of pV_3D_3 films

The pristine pV_3D_3 film was deposited on Si wafer in a custom-built iCVD reactor. The liquid monomer 1,3,5-trivinyl-1,3,5-trimethylcyclotrisiloxane (V_3D_3 , TCI, >95%) and the initiator tert-butyl peroxide (TBPO, Aladdin, 97%) were utilized without further purification. During the deposition, the V_3D_3 monomer was heated at 70 °C to generate sufficient vapor pressure for delivery to the iCVD chamber at a flow rate of 0.90 ± 0.02 sccm. The initiator was kept at room temperature, and delivered at a flow rate of 0.59 ± 0.01 sccm. The chamber pressure was controlled at 200 mTorr by a butterfly valve. In a typical iCVD process, the temperature of heated filaments was controlled at 250 °C, while the sample stage was kept at 30 °C by a chiller. The TBPO initiator was cleaved to form free radicals by the heated filaments, which then reacted with the adsorbed monomer on the substrate to initiate polymerization. The synthesis process is presented in figure 1.

The iCVD deposited pV_3D_3 film was annealed in ambient air in a muffle furnace. During the annealing process, the furnace temperature was slowly ramped up at a rate of $10 \text{ }^\circ\text{C min}^{-1}$. After annealing for 1 h, the resulting film was

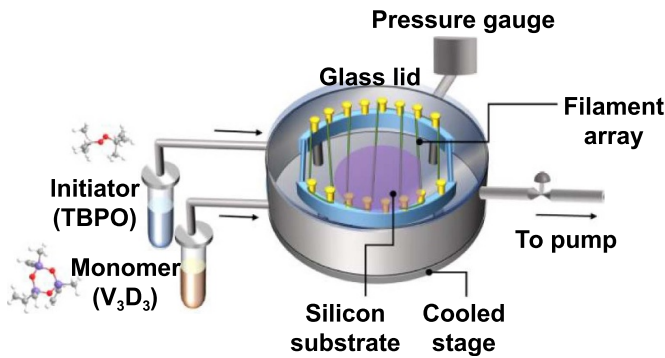


Figure 1. Schematic illustration of an iCVD reactor.

cooled down to room temperature and then collected from the furnace. We investigated the annealing temperatures of 200 °C, 400 °C, 550 °C, 700 °C and 850 °C.

2.2. Materials characterization

The morphology of the pristine film and annealed films were characterized using scanning electron microscopy (SEM, SU-8010, Hitachi) and atomic force microscopy (AFM, Dimension Icon, Bruker). The AFM measurements were performed in tapping mode over an area of $5 \mu\text{m} \times 5 \mu\text{m}$. The thickness of the pristine film and annealed films was measured utilizing a profilometer (DEKTAK-XT, Bruker).

Attenuated total reflectance-FTIR spectra were recorded with a Nicolet iS50 (ThermoFisher Scientific) using a DTGS-KBr detector. Measurements were carried out over the wavenumber range of $400\text{--}4000 \text{ cm}^{-1}$ with a resolution of 4 cm^{-1} .

XPS analysis was carried out on a ThermoFisher photoelectron spectrometer (ESCALAB Xi+) to analyze the chemical composition of the films. A monochromated Al $K\alpha$ X-ray source (1486.6 eV; $500 \mu\text{m}$; 500 W) was used as the excitation source. High resolution spectra were captured using a pass energy of 20 eV with step size of 0.1 eV. All data were charge-corrected to C 1s at 284.5 eV. Avantage software was used to process the XPS data.

XRR measurements were performed using a Rigaku Smartlab X-ray diffractometer (Cu $K\alpha$ X-ray source). The incident angle below which total reflection occurs is referred as the critical angle, θ_c . The mass density ρ can be calculated from θ_c through the following equation

$$\frac{\theta_c^2}{\rho} = \frac{r_e \lambda^2 Z N_A}{\pi A} \quad (1)$$

where r_e is the classical electron radius ($2.82 \times 10^{-15} \text{ m}$), λ is the X-ray wavelength, Z is the atomic number, N_A is the Avogadro's number, and A is the mass number.

2.3. Nanoindentation

The hardness and modulus of the pristine and annealed pV₃D₃ films were carried out using a Keysight G200 nanoindenter. Continuous stiffness measurements with a frequency of 75 Hz

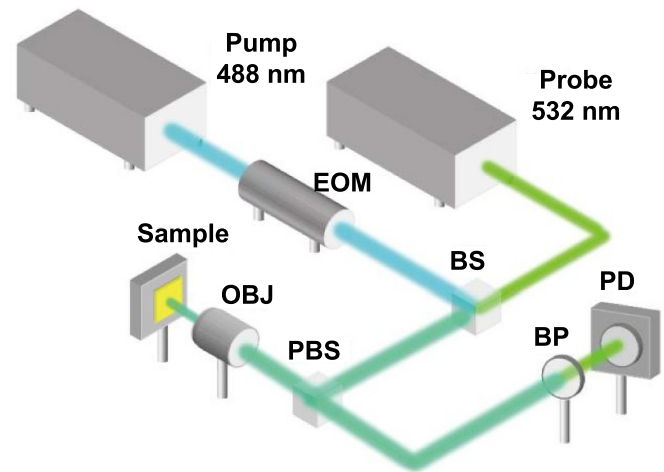


Figure 2. Schematic of the FDTR setup. The abbreviations are EOM (electro-optic modulator), BS (beam splitter), PBS (polarized beam splitter), OBJ (objective lens), BP (bandpass filter), and PD (photodiode detector).

and a displacement amplitude of 1 nm were adopted for analyzing the mechanical properties. A Berkovich diamond tip was indented into the sample with a strain-rate of 0.05 s^{-1} . To minimize the substrate effect, the hardness and modulus are reported at the depth of ca. 10% of the film thickness.

2.4. FDTR

The thermal conductivity of pV₃D₃ films at room temperature was measured using the FDTR [31, 32]. The pristine and annealed pV₃D₃ films grown on the silicon substrate were first coated with 70 nm of gold to improve the optical reflectance signal. As shown in figure 2, our FDTR setup uses an intensity-modulated pump laser (488 nm) to heat the sample surface periodically. A 532 nm green laser probes the resulting temperature response on the gold surface. The phase lag between the pump laser (heat flux) and the probe laser (temperature rise) is recorded by a lock-in amplifier over frequencies ranging from 60 kHz to 5.2 MHz. The thermal properties of the pV₃D₃ samples were then extracted by fitting the phase lag data to the multilayer heat conduction model [33].

The input properties of the gold, pV₃D₃ films, and silicon for the multilayer heat conduction model are characterized separately or obtained from the literature. The thickness of the gold layer and pV₃D₃ films were measured by a profilometer. The thermal conductivity of the gold layer was calculated using the Wiedemann–Franz law after its electrical conductivity was measured using a four-point probe. The thermal conductivity of the silicon substrate was determined by separate FDTR measurements. Details of the FDTR fit can be found in the supplementary information.

2.5. Wear resistance test

The wear resistance performance of the pristine pV₃D₃ coating and the PDC film derived from annealing at 850 °C were evaluated through a tribology system (UMT-2, Bruker) at room

temperature. A constant load of 5 N was applied by a friction pair, which was composed of friction surface of $\Phi 3$ mm alumina ball. After the load was applied, the sample was cycled in a reciprocating motion with a speed of 60 mm s^{-1} and a travel distance of 20 mm. After 30 min, the surface morphology and the bulk worn loss were obtained by an optical profiler (MicroXAM-800, KLA-Tensor). The wear rate was calculated based on the net volume worn loss obtained from the optical profiler. More calculation details can be found in the supplementary information. The mass loss was obtained by weighing the mass before and after the wear using an analytical balance (Mettler Toledo).

3. Results and discussion

3.1. Structure transition

The morphology of the pristine iCVD pV_3D_3 and the annealed films were carried out using SEM and AFM (figure 3). The pristine film (figure 3(a)) exhibits a low surface roughness of 0.53 nm, similar to prior reports [34]. The film thickness (390 nm) measured from the cross-sectional SEM (figure 3(g)) corresponds to a deposition rate of 0.8 nm min^{-1} . No cracks or other defects were observed after thermal annealing at different temperatures. The surface roughness of the films annealed at different temperatures ranges from 0.39 nm to 0.61 nm, which is similar to the pristine pV_3D_3 film. The film thickness was found to decrease after annealing at 400°C and 800°C (figures 3(h) and (i)), which agrees with the past reports on PDC films [13, 18].

Figure 4(a) shows the FTIR spectra for the pristine and annealed pV_3D_3 films. For the as-deposited pV_3D_3 thin film, the peak at 1003 cm^{-1} is associated with the asymmetric stretching of Si–O–Si [22, 35]. The absorption band at 740 cm^{-1} is attributed to Si–O–Si symmetric stretching mode ($\nu_s(\text{Si–O–Si})$), while the band at 795 cm^{-1} is attributed to Si–CH₃ rocking ($\rho(\text{Si–CH}_3)$) in D units [O_2SiR_2] [36]. In addition, the characteristic peak at 1260 cm^{-1} represents the Si–CH₃ symmetric bending mode ($\delta_s(\text{Si–CH}_3)$) of D units [29, 37]. The wagging mode of CH₂ ($\omega(\text{CH}_2)$) in the pendant vinyl groups appears at 970 cm^{-1} , which is consistent with the previous reports for iCVD pV_3D_3 [38].

After annealing at 200°C , the decrease of absorbance at 970 cm^{-1} of pV_3D_3 indicates the increased degree the cross-linking for the pendant vinyls [39]. Complete conversion of the pendant vinyls after annealing at 400°C was confirmed by FTIR, as the $\omega(\text{CH}_2)$ at 970 cm^{-1} disappeared.

The absorbance of the $\rho(\text{Si–CH}_3)$ at 795 cm^{-1} in the D units of pV_3D_3 was found to decrease after the film was annealed at temperature range from 400°C to 550°C . The new absorption peak at 780 cm^{-1} can be attributed to the $\rho(\text{Si–CH}_3)$ and $\nu(\text{Si–C})$ modes in T groups [36]. Additionally, compared with the pristine and the annealed pV_3D_3 at 200°C , the $\delta_s(\text{Si–CH}_3)$ peak shifted from 1260 cm^{-1} to 1273 cm^{-1} , which is another clear evidence for the conversion from D units to T units [29, 40].

The $\nu_{\text{as}}(\text{Si–O–Si})$ peak of the pristine pV_3D_3 evolved into multiple peaks at a higher wavenumber range (from 1032 to 1130 cm^{-1}) after annealing at 400°C – 550°C , suggesting changes in the Si–O–Si bonds. Previous reports have found that the $\nu_{\text{as}}(\text{Si–O–Si})$ shifts to higher wavenumbers with increased Si–O–Si bond angles ($\angle_{\text{Si–O–Si}}$) [36]. Here, the absorption peaks at 1032 cm^{-1} , 1060 cm^{-1} , and 1130 cm^{-1} are assigned to strained siloxane rings ($\angle_{\text{Si–O–Si}} < 140^\circ$), networks ($\angle_{\text{Si–O–Si}} \approx 140^\circ$), and cage structures ($\angle_{\text{Si–O–Si}} \approx 150^\circ$), respectively [36]. These results indicate the oxidation of the alkyl groups on the D units and the formation of Si–O–Si bridges (figure 4(b)). For annealing temperatures $\geq 700^\circ\text{C}$, the two broad peaks at 1060 and 1180 cm^{-1} indicate the generation of Q units [O_4Si] [41] and therefore silica-like structures [42].

Figure 5(a) represents the contents of C, O and Si in the pristine and annealed pV_3D_3 films determined by XPS. The C concentration was found to decrease with the rise of the annealing temperature. The pristine pV_3D_3 contained 55% of C, while the C content reduced to 46%, 24%, 17%, 8% and 5% for the films annealed at 200°C , 400°C , 550°C , 700°C and 850°C , respectively. The proportion of O substantially increased from 23% in the pristine pV_3D_3 film to 59% in the film annealed at 850°C , which reflects the gradual oxidation process during the thermal annealing in air.

As shown in figure 5(b), the shifts of Si 2p towards larger binding energy reveal the changes of siloxane structures. According to O'Hare *et al* [43], four types of siloxanes correspond to different binding energies: mono-functional (M) units at 101.4 eV, di-functional (D) units at 102.0 eV, tri-functional (T) units at 102.8 eV, and quad-functional (Q) units at 103.2 eV. After the C 1s spectrum was charge-corrected to 284.5 eV, the deconvolution of Si 2p peaks (figures 5(c)–(g)) allowed us to determine the composition [44].

Figure 5(h) shows the percentages of D, T and Q units among all the siloxane moieties in the pristine and annealed pV_3D_3 films processed at different temperatures. With increased annealing temperature, the fraction of D units decreased from 100% in the pristine film to 10% in the annealed film at 850°C . Notice that a rapid drop of D percentage was found for the annealing condition of 400°C , accompanied with substantially increased amount of T groups as well as newly-formed Q groups. These results agree well with the FTIR data and indicate that most of the D groups were converted in the temperature window below 400°C .

We found that the primary source for Q units is through the conversion from T groups. The gradual increase of T percentage to 56% below 400°C and the subsequent decrease down to 0% at higher temperatures in figure 5(h) indicate that T units are not stable in an oxidative, high-temperature condition. Noticeably, dramatic changes in T and Q percentages were found in the temperature range from 550°C to 700°C , while the amount of D units was only reduced by 4% in the same temperature range. These results, together with the fact that the generation of Q units lagged behind T units, confirm that the Q units mainly resulted from the oxidation of T units.

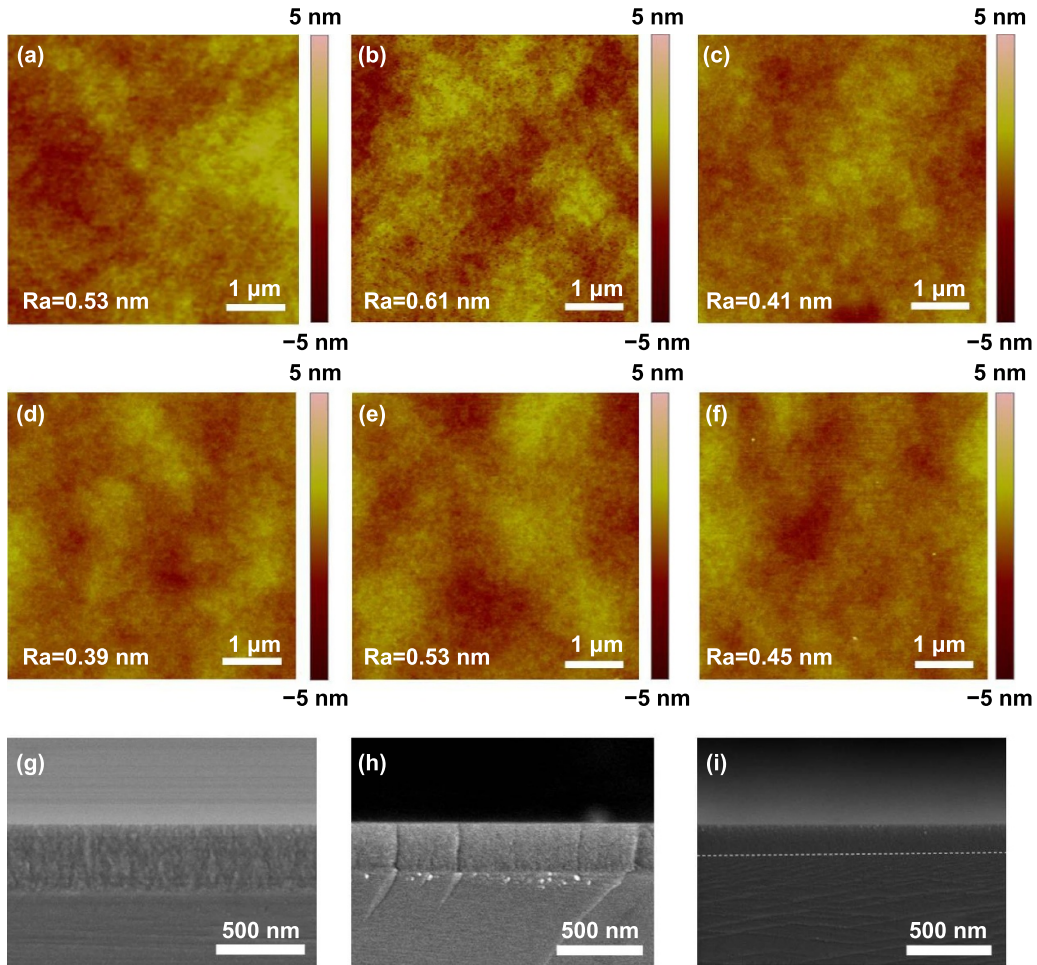


Figure 3. Morphology of the pristine and annealed pV_3D_3 films. AFM images ($5 \mu\text{m} \times 5 \mu\text{m}$) of (a) pristine pV_3D_3 film and the films annealed at (b) 200°C , (c) 400°C , (d) 550°C , (e) 700°C , and (f) 850°C . Cross-sectional SEM images of (g) pristine film and films annealed at (h) 400°C and (i) 850°C . The dashed line in (i) indicates the interface between the film and the Si substrate.

Compared with D units which can only form siloxane chains or rings, the evolution of T and Q units enables the formation of 3D network and cage structures. Such structural evolution can be quantified by the connectivity number $\langle r \rangle$, which has been defined as the average ratio of network-forming bonds to network-forming atoms in a polymeric structure [29, 45–47]. We first adopted the connectivity number reported for an organosilicate glass film with $\text{Si}_x\text{O}_y(\text{CH}_3)_z$ formula [40], where the relative fractions x , y , and z can be determined via XPS and FTIR

$$\langle r \rangle = \frac{(4x - z) + 2y}{x + y}. \quad (2)$$

The calculated connectivity number for the pristine and annealed pV_3D_3 films are shown in figure 5(i). The $\langle r \rangle$ value increased as a function of the annealing temperature. Noticeably, a sharp rise of the $\langle r \rangle$ value to 2.48 was found in the temperature range from 200°C to 400°C , possibly because of the rapid evolution of T and Q units in the annealed pV_3D_3 . This connectivity transition occurred at lower temperature

than the range reported for pV_4D_4 (400°C to 600°C) [30], indicating that the strained, six-membered rings in pV_3D_3 [48] are more prone to form highly connected topologies at mild annealing conditions than the eight-membered rings in pV_4D_4 .

We found that the structural evolution of pV_3D_3 at high annealing temperatures complicates the determination of the connectivity number. The assumption of all C atoms in form of methyl groups in equation (2) may not be valid for high process temperatures (e.g. $\geq 700^\circ\text{C}$). Instead of being terminal points with negative contribution towards the connectivity number, the carbon atoms may form tetrahedron structures with four Si–C bonds which positively contribute to the connectivity number. Assuming that all the remaining C atoms in the annealed films exist in the form of Si_4C , we propose a modified connectivity number for annealed PDC films with a $\text{Si}_x\text{O}_y\text{C}_z$ formula:

$$\langle r \rangle = \frac{4x + 2y + 4z}{x + y + z}. \quad (3)$$

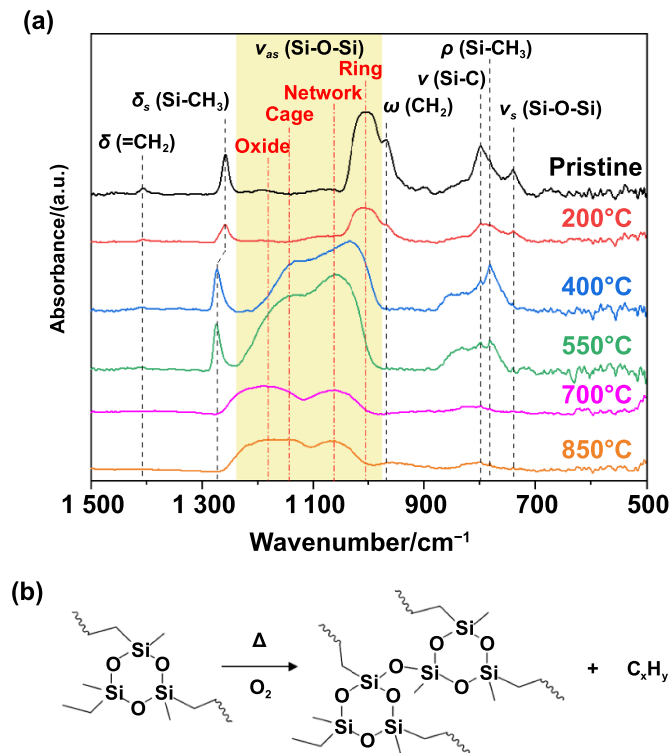


Figure 4. Structural evolution of the pristine and annealed pV₃D₃ films. (a) FTIR spectra of the pristine and annealed pV₃D₃ films. Absorption peaks are associated with major vibration modes: ν stretching, ρ rocking, δ bending, ω wagging, s symmetric, and as asymmetric vibrations. (b) Proposed reaction route for the formation of Si–O–Si bridges between the cyclosiloxane rings.

The $\langle r \rangle$ value defined in equation (2) provides lowest estimation for the connectivity number, while the modified $\langle r \rangle$ value in equation (3) gives the upper limit for the connectivity number, because free forms of carbon with no contribution to the connectivity has also been reported in PDCs [13]. Accordingly, the connectivity number range estimated for the films annealed at 700 °C and 850 °C were 2.68–2.88, and 2.70–2.86, respectively.

We measured the density of the pV₃D₃ films using XRR (figure 6), and found step increases with the rise of annealing temperature. The density of the pristine pV₃D₃ film was $1.24 \pm 0.02 \text{ g cm}^{-3}$, similar to the previous reports [26, 49]. After the film was annealed at 200 °C, the density remained the same as the pristine film. The film density rose to $1.44 \pm 0.03 \text{ g cm}^{-3}$ after annealing at 400 °C, while another jump in the film density to $2.10 \pm 0.06 \text{ g cm}^{-3}$ was observed in the temperature range between 550 °C and 700 °C. We calculated the film thickness retention based on the profilometer data acquired before and after thermal annealing (figure 6, see details in table S1), which agrees with the change of film density. The step changes in film density, together with the FTIR and XPS analysis, suggest the following three-stage mechanism for the structural evolution during thermal annealing (figure 7):

(i) Crosslinking of pendant vinyls, and slow oxidation of D units to T units were mainly involved in the first stage of thermal annealing for pV₃D₃.

(ii) Cleavage of C–C bonds in the polymer backbones, rapid oxidation from D units to T units, and partial conversion of T units to Q units occurred in the second stage.

(iii) Complete oxidation of T units to Q units was the primary reaction in the third stage during the thermal annealing process.

3.2. Enhanced mechanical properties

Enhancement of Young's modulus and hardness were found after the pV₃D₃ films were annealed. Figures 8(a) and (b) represent the modulus and hardness versus displacement curves plotted for the pristine and annealed films. Continuous stiffness methods were utilized in the nanoindentation measurements, and the Young's modulus and hardness (figure 8(c)) were reported at 10% of the film thickness to remove substrate contribution [50].

The Young's modulus and hardness of the pristine film were $6.3 \pm 0.3 \text{ GPa}$ and $0.41 \pm 0.02 \text{ GPa}$, respectively, which agree well with the previously reported value [48]. The changes in the mechanical properties for the pV₃D₃ films annealed at 200 °C were negligible. The Young's modulus increased to $6.7 \pm 0.2 \text{ GPa}$ at 400 °C and $13.1 \pm 0.3 \text{ GPa}$ at 550 °C, respectively. Improvement of film hardness by over 100% was also found at annealing temperatures $\geq 400 \text{ °C}$.

These changes in the mechanical properties can be explained by the rise of the connectivity number [29, 40]. The connectivity number for the pristine and the annealed pV₃D₃

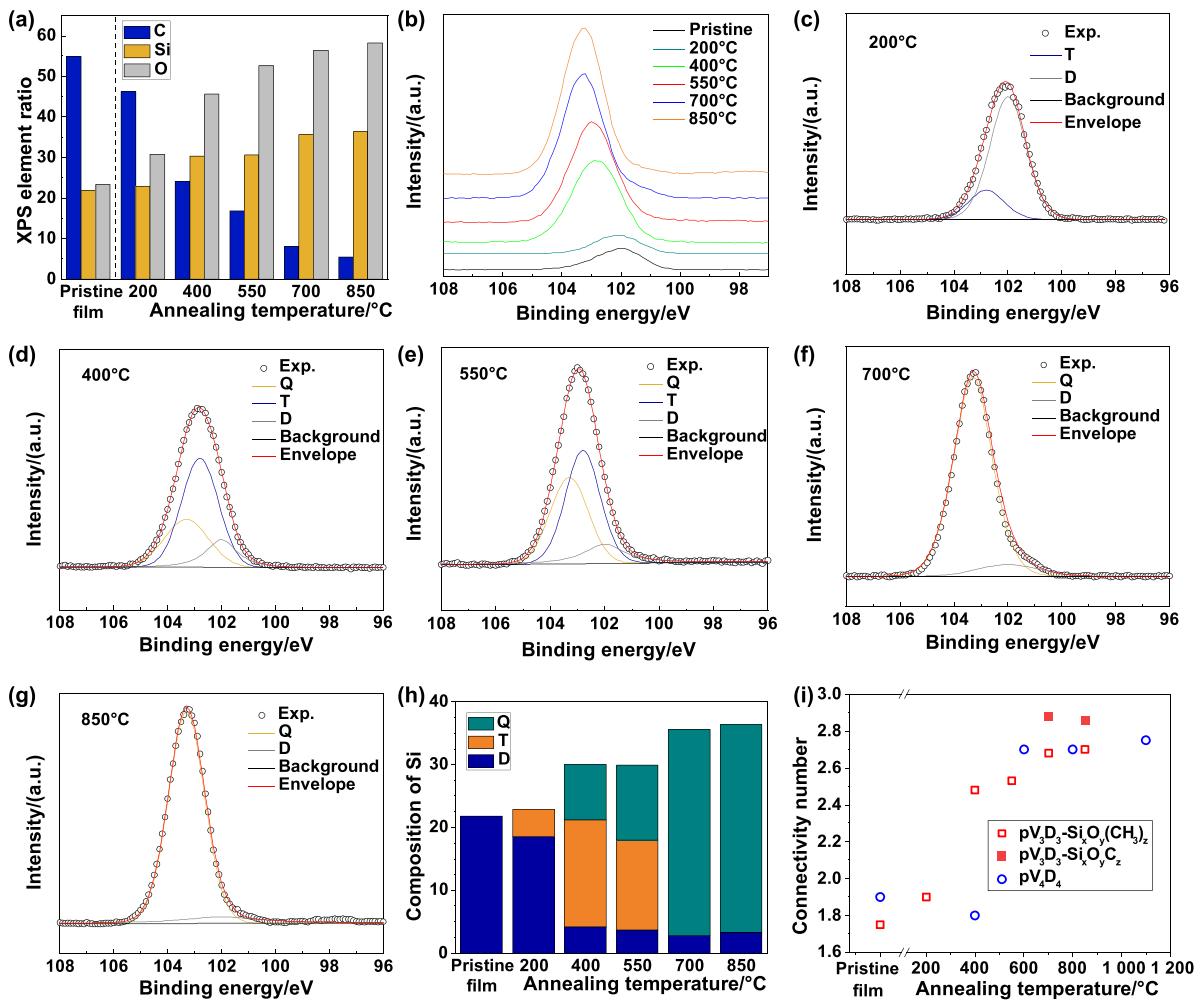


Figure 5. Changes in the composition of the pristine and annealed pV₃D₃ films. (a) XPS element ratio of pristine film and films at different annealing temperatures. (b) XPS binding energy shifts of Si 2p with different annealing temperatures. (c)–(g) Curve-fits for the Si 2p core level of films annealed at (c) 200 °C, (d) 400 °C, (e) 550 °C, (f) 700 °C, and (g) 850 °C. (h) Proportions of D, Q and T units among the siloxane groups in the pristine and annealed films. (i) Connectivity number of pV₃D₃ and pV₄D₄ films (blank red square for pV₃D₃ calculated using equation (2), filled red square for pV₃D₃ calculated using equation (3), blank blue circle for pV₄D₄ calculated using equation (2) from [30]).

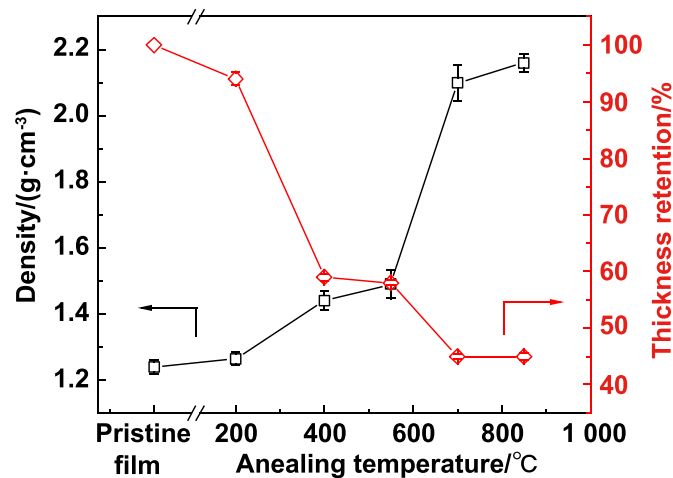


Figure 6. Density (black square) and thickness retention (red diamond) of the pristine and annealed pV₃D₃ films.

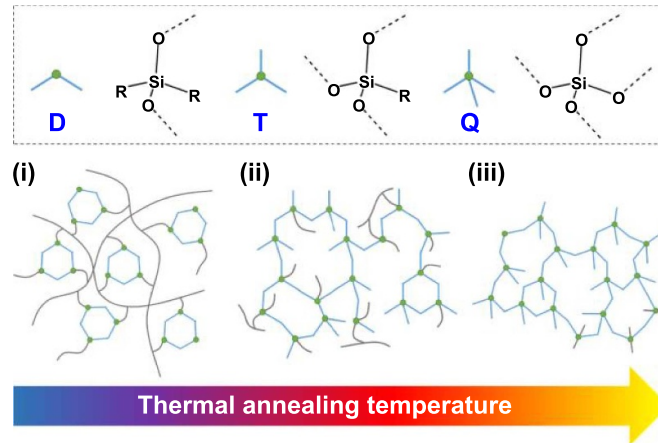


Figure 7. Proposed structure changes during thermal annealing process.

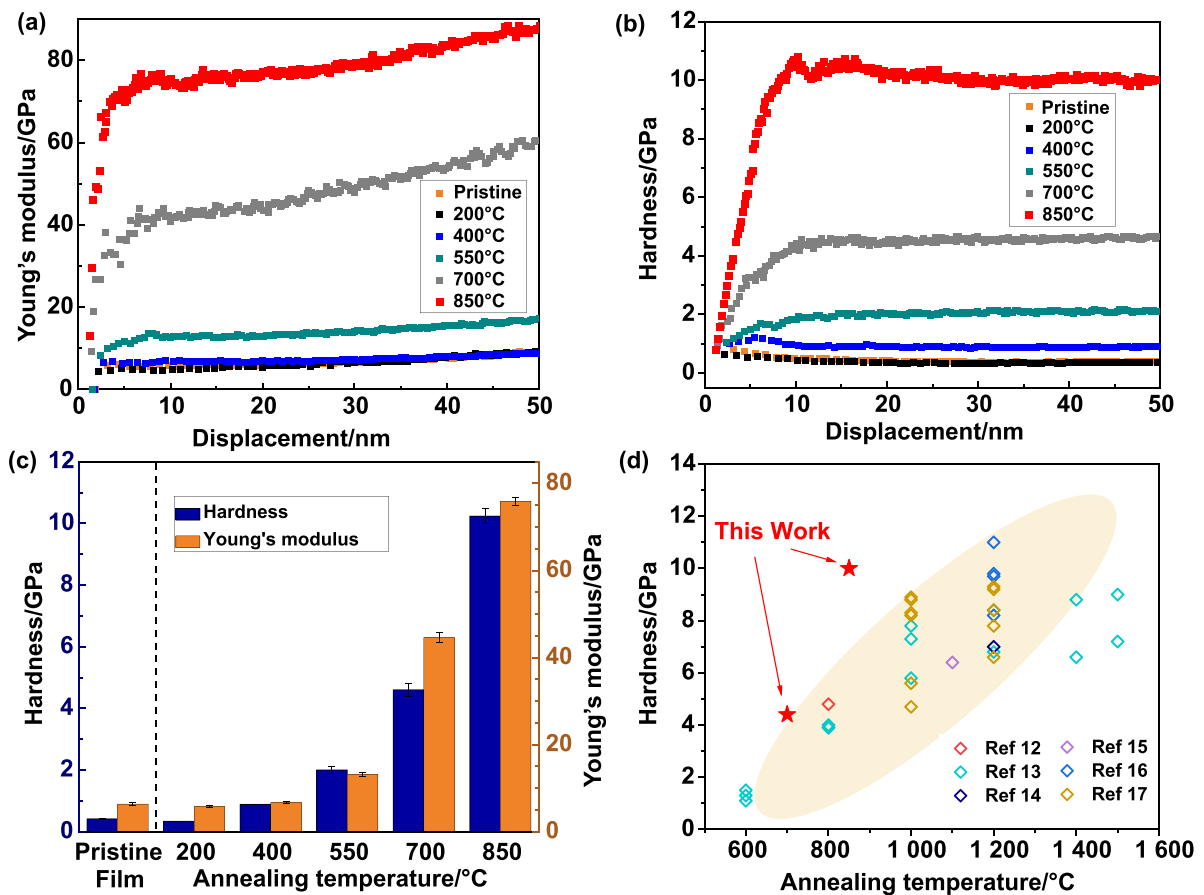


Figure 8. Enhanced mechanical properties of the pristine and annealed pV₃D₃ films. (a) Young's modulus and (b) hardness of the pristine film and films at different annealing temperature as a function of indent displacement. (c) Average values of the Young's modulus and hardness versus annealing temperature. (d) A comparison between this work and previous reported hardness for the PDC films obtained at different annealing temperatures.

at 200 °C were below the percolation of rigidity, which was defined as a composition transition point at $\langle r \rangle = 2.4$ [51]. Such systems can be considered as underconstrained or nonrigid state with low sensitivity of mechanical properties towards the topological changes. In comparison, the connectivity number for the films annealed at temperatures ≥ 400 °C were above

the percolation threshold, which reflects the transition into the overconstrained or rigid state. Consequently, Young's modulus becomes sensitive to changes in the connectivity number, exhibiting a power dependence on the connectivity number beyond the rigidity percolation threshold [52, 53]. Indeed, we found a significant boost in the mechanical properties for the

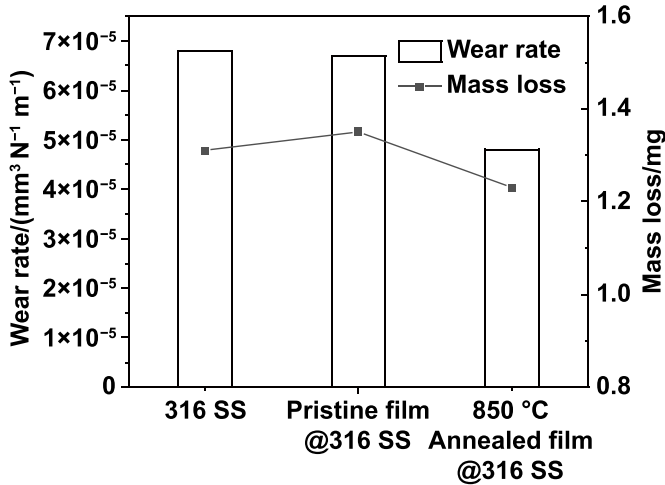


Figure 9. Wear rate and mass loss of 316 SS sheets without coating, with pristine pV_3D_3 coating, and with PDC coating obtained via annealing at 850 °C.

films annealed at 700 °C and 850 °C. The Young's modulus was 44.6 ± 1.0 GPa at 700 °C, and 75.9 ± 0.9 GPa at 850 °C, respectively.

We compared our hardness results with those previously reported PDCs in figure 8(d). Our coatings obtained via annealing at 850 °C show at least 14.6% higher hardness than previously reported PDCs annealed at the temperature ≤ 1100 °C, indicating the possibility to achieve durable PDC coatings for engineering metal materials with low melting points. The enhanced mechanical properties can be explained by the Si–O–Si bridges formed by the participation of oxygen in thermal annealing to increase the network connectivity [29, 40], and the replacement of carbon by oxygen to avoid the generation of free carbon regions which have been reported to decrease the mechanical properties of PDCs [13, 54].

Wear test was carried out on a tribology system [55–57]. The wear resistance of uncoated 316 stainless steel (316 SS) was compared with 316 SS with unannealed pV_3D_3 coating, and 316 SS with PDC coating derived from annealing iCVD pV_3D_3 at 850 °C. The wear rate of 316 SS was $6.8 \times 10^{-5} \text{ mm}^3 \text{N}^{-1} \text{m}^{-1}$ (sliding speed of 60 mm s^{-1} , 5 N of applied load), which is similar to the data obtained under similar friction conditions in literature ($6.2 \times 10^{-5} \text{ mm}^3 \text{N}^{-1} \text{m}^{-1}$, sliding speed of 25 mm s^{-1} , 6 N of applied load) [58]. The wear rate of 316 SS with the unannealed pV_3D_3 coating was found similar to the uncoated 316 SS, while our PDC coating reduced the wear rate by 23% to $4.8 \times 10^{-5} \text{ mm}^3 \text{N}^{-1} \text{m}^{-1}$. Moreover, compared with the mass loss (1.31 mg) of the uncoated 316 SS due to the wear test, PDC-coated 316 SS also exhibited a 24% lower mass loss (1.23 mg) after testing (figure 9). These results indicate good wear resistance of our PDC film derived from annealing iCVD pV_3D_3 at 850 °C.

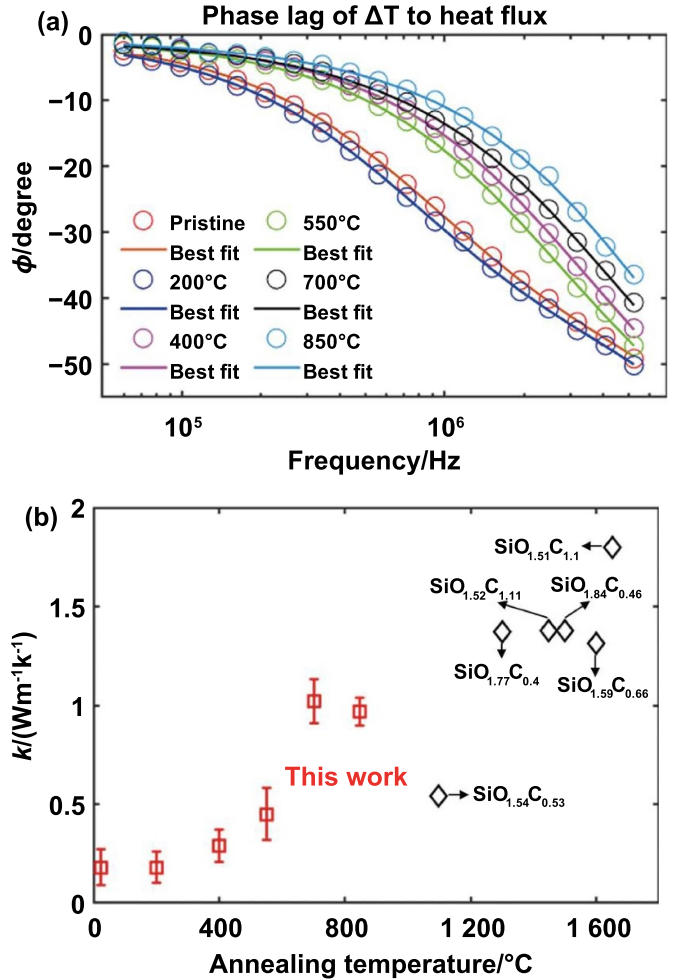


Figure 10. Thermal conductivity of the pristine and annealed pV_3D_3 films. (a) Experimentally measured FDTR phase lags and the best-fit curves. (b) The measured thermal conductivity versus annealing temperature for various PDC materials ($\text{SiO}_{1.52}\text{C}_{1.11}$ and $\text{SiO}_{1.51}\text{C}_{1.10}$ from [62], $\text{SiO}_{1.77}\text{C}_{0.4}$ and $\text{SiO}_{1.84}\text{C}_{0.46}$ from [63], $\text{SiO}_{1.54}\text{C}_{0.53}$ and $\text{SiO}_{1.59}\text{C}_{0.66}$ from [64]).

3.3. Improved thermal conductivity

We employed the FDTR technique to analyze the thermal conductivity of the pristine and annealed pV_3D_3 films. Their thermal conductivity and volumetric heat capacity were extracted by fitting the measured phase lag to the heat conduction model, as plotted in figure 10(a). The interfacial thermal conductance between the gold and pV_3D_3 films was assumed as $50 \text{ MW (m}^2\text{K)}^{-1}$ (a typical value for a metal–amorphous interface) [59–61]. The exact magnitude has minimal effect on the results due to its low sensitivity (see details in the supplementary information).

The measured thermal conductivity values of the pV_3D_3 films are presented in figure 10(b), together with some other PDC materials. As the annealing temperature increases from room temperature (pristine) to 700 °C, the thermal conductivity increases by approximately six-fold from 0.18 to

1.02 W (mK)^{-1} . The main change occurs in the temperature range from $550 \text{ }^\circ\text{C}$ to $700 \text{ }^\circ\text{C}$, suggesting a significant structural change. Compared with other PDC materials, the thermal conductivity of our pV_3D_3 films annealed at $700 \text{ }^\circ\text{C}$ reached a similar order of magnitude as other PDCs treated above $1100 \text{ }^\circ\text{C}$.

As the pV_3D_3 films are inherently disordered, we compared the measured thermal conductivity values with the theoretical results from two thermal conductivity models used often for amorphous materials, i.e. the Cahill–Pohl model [65] and the diffuson-mediated model [66]. The Cahill–Pohl minimum thermal conductivity limit is given by

$$k_{\min} = \left(\frac{\pi}{6}\right)^{1/3} k_{\text{B}} n^{2/3} \sum_i v_i \left(\frac{T}{\Theta_i}\right)^2 \int_0^{\Theta_i/T} \frac{x^3 e^x}{(e^x - 1)^2} dx. \quad (4)$$

The summation in equation (4) is over the two transverse (i.e. $i = T$) and one longitudinal (i.e. $i = L$) acoustic modes, n is the number density of atoms, v_i is the sound speed, and $\Theta_i = v_i (\hbar/k_{\text{B}}) (6\pi^2 n)^{1/3}$ is the Debye temperature of the i th polarization mode. This model treats the heat carriers as phonon particles with a maximum mean free path of each phonon to be half of its wavelength. Following the Allen–Feldman theory [67] and considering the heat transport as entirely driven by the diffusons, Agne *et al* derived the room-temperature diffuson-mediated minimum thermal conductivity for amorphous materials as

$$k_{\text{diff}} = 0.61 \frac{n^{1/3} k_{\text{B}}^2 \Theta_{\text{D}}}{\pi \hbar} \quad (5)$$

where $\Theta_{\text{D}} = v_{\text{s}} (\hbar/k_{\text{B}}) (6\pi^2 n)^{1/3}$ is the Debye temperature calculate from the arithmetic average sound speed, $v_{\text{s}} = \frac{1}{3}(2v_{\text{T}} + v_{\text{L}})$. This expression is derived by assuming the maximum value for diffuson diffusivity [66].

In both models, the calculation requires the sound speed and number density of atoms in the material. In this study, we calculated the sound speed and number density of atoms from the XRR-derived density, the nanoindentation-derived Young's modulus, and the XPS elemental ratio (see details in supplementary materials). Figure 11 shows the comparison between the experimental and the theoretical values, with the light blue shaded area representing the composition transition region (i.e. $2.4 < \langle r \rangle < 2.5$) [52, 53]. A polymer is underconstrained and soft below 2.4, while overconstrained and rigid when above 2.4. Our thermal conductivity trend exhibits a similar bifurcation behavior separated by this transition region. When annealed at temperatures below $400 \text{ }^\circ\text{C}$, the thermal conductivity of the pV_3D_3 films is better described using the diffuson-mediated model. This result suggests that the diffusons carry heat in the underconstrained pV_3D_3 , imparting a very low thermal conductivity. The experimental results in this region are a bit lower than the calculated diffuson-mediated results that used the maximum diffuson diffusivity, probably due to some localized vibrational modes (locons) that contribute to the heat capacity but not to the thermal transport. On the other hand, when annealed at temperatures above $550 \text{ }^\circ\text{C}$, the

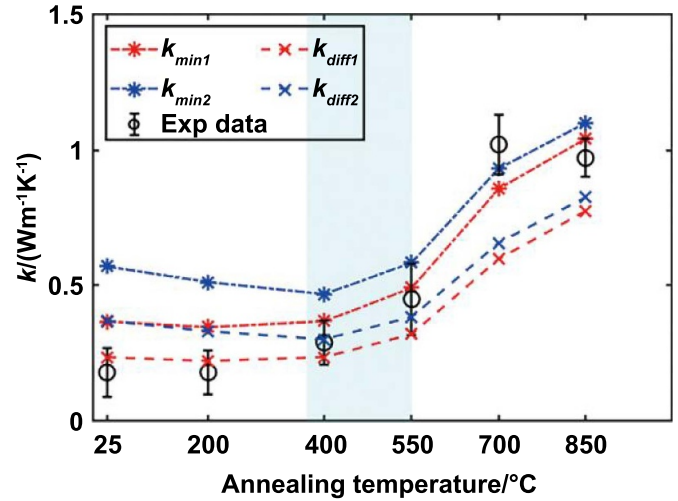


Figure 11. Cahill–Pohl thermal conductivity limit k_{\min} (star), diffuson-mediated minimum thermal conductivity k_{diff} (cross), together with the experimental data (circles) of pV_3D_3 annealed at various temperatures. Subscript 1 represents zero hydrogen element limit, and subscript 2 represents maximum hydrogen element limit (element ratio of carbon to hydrogen is 1:2, as in a monomer V_3D_3). The shaded region indicates the composition transition region with the $\langle r \rangle$ value between 2.4 and 2.5.

measured thermal conductivity values increased and became more consistent with predictions from the Cahill–Pohl model. This result, perhaps, indicates that phonons at the maximum scattering limit facilitate the thermal transport in this overconstrained region. This change in the transport mechanism reflects the changes in the structure, as a more extensively linked network is created after annealing at a higher temperature. For the shaded region, the thermal transport transits from a diffuson-dominated process to one with increased participation of ultra-short mean-free path phonons. This transition will require further investigation, although a similar trend was reported recently for amorphous chalcogenides [68].

4. Conclusions

In conclusion, we have developed a new synthesis route for PDC films using iCVD pV_3D_3 as the precursor template. Changes in the composition of siloxane (D, T and Q) unites and the network topology of the pV_3D_3 films after thermal annealing reveal a three-stage reaction mechanism at low, middle and high temperature zones. We found that the increase of the connectivity number endowed the improvement in mechanical properties and thermal conductivity. Compared with the previously reported PDCs synthesized below $1100 \text{ }^\circ\text{C}$, our pV_3D_3 films annealed at $850 \text{ }^\circ\text{C}$ exhibit at least 14.6% higher hardness. Furthermore, we achieved thermal conductivity up to 1.02 W (mK)^{-1} , which is on the same order of magnitude as PDCs obtained above $1100 \text{ }^\circ\text{C}$. The measured thermal conductivity has also been well described by the minimum thermal conductivity models for amorphous materials. The process developed here and the key findings in this

work are expected to promote the future development of wear-resistant and thermally conductive PDC coatings.

Acknowledgments

We acknowledge the funding from the National Natural Science Foundation of China (22178301, 21938011, 51876186 and 52150410417) and the funding from the National Science Foundation of Zhejiang Province (LR21B060003 and LZ19E060002). J Z acknowledges the grant from Science Technology Department of Zhejiang Province (2023C01182). This work is also supported by Shanxi Institute of Zhejiang University for New Materials and Chemical Industry (2022SZ-TD005).

ORCID iDs

Wee-Liat Ong  <https://orcid.org/0000-0003-3035-6991>

Junjie Zhao  <https://orcid.org/0000-0001-6205-9671>

References

- Colombo P, Mera G, Riedel R and Soraru G D 2010 Polymer-derived ceramics: 40 years of research and innovation in advanced ceramics *J. Am. Ceram. Soc.* **93** 1805–37
- Barrios E and Zhai L 2020 A review of the evolution of the nanostructure of SiCN and SiOC polymer derived ceramics and the impact on mechanical properties *Mol. Syst. Des. Eng.* **5** 1606–41
- Greil P 2000 Polymer derived engineering ceramics *Adv. Eng. Mater.* **2** 339–48
- Wang K S, Unger J, Torrey J D, Flinn B D and Bordia R K 2014 Corrosion resistant polymer derived ceramic composite environmental barrier coatings *J. Eur. Ceram. Soc.* **34** 3597–606
- Riffard F, Joannet E, Buscail H, Rolland R and Perrier S 2017 Beneficial effect of a pre-ceramic polymer coating on the protection at 900 °C of a commercial AISI 304 stainless steel *Oxid. Met.* **88** 211–20
- Hasemann G, Baumann T, Dieck S, Rannabauer S and Krüger M 2015 Polymer-derived ceramics as innovative oxidation barrier coatings for Mo–Si–B alloys *Metall. Mater. Trans. A* **46** 1455–60
- Torrey J D and Bordia R K 2007 Phase and microstructural evolution in polymer-derived composite systems and coatings *J. Mater. Res.* **22** 1959–66
- Torrey J D and Bordia R K 2008 Processing of polymer-derived ceramic composite coatings on steel *J. Am. Ceram. Soc.* **91** 41–45
- Kraus T, Günthner M, Krenkel W and Motz G 2009 cBN particle filled SiCN precursor coatings *Adv. Appl. Ceram.* **108** 476–82
- Liu M-Y, Wang H and Wang Y 2007 Enhancing flow boiling and antifouling with nanometer titanium dioxide coating surfaces *AIChE J.* **53** 1075–85
- Szymanski W, Lipa S, Fortuniak W, Chojnowski J, Pospiech P, Mizerska U, Slomkowski S, Nyczyk-Malinowska A and Hasik M 2019 Silicon oxycarbide (SiOC) ceramic microspheres—structure and mechanical properties by nanoindentation studies *Ceram. Int.* **45** 11946–54
- Torrey J D and Bordia R K 2008 Mechanical properties of polymer-derived ceramic composite coatings on steel *J. Eur. Ceram. Soc.* **28** 253–7
- Walter S, Soraru G D, Bréquel H and Enzo S 2002 Microstructural and mechanical characterization of sol gel-derived Si–O–C glasses *J. Eur. Ceram. Soc.* **22** 2389–400
- Renlund G M, Prochazka S and Doremus R H 1991 Silicon oxycarbide glasses: part II. structure and properties *J. Mater. Res.* **6** 2723–34
- Moysan C, Riedel R, Harshe R, Rouxel T and Augereau F 2007 Mechanical characterization of a polysiloxane-derived SiOC glass *J. Eur. Ceram. Soc.* **27** 397–403
- Soraru G D, Kundanati L, Santhosh B and Pugno N 2019 Influence of free carbon on the Young's modulus and hardness of polymer-derived silicon oxycarbide glasses *J. Am. Ceram. Soc.* **102** 907–13
- Soraru G D, Dallapiccola E and D'Andrea G 1996 Mechanical characterization of sol–gel-derived silicon oxycarbide glasses *J. Am. Ceram. Soc.* **79** 2074–80
- Janakiraman N and Aldinger F 2009 Fabrication and characterization of fully dense Si–C–N ceramics from a poly(ureamethylvinyl)silazane precursor *J. Eur. Ceram. Soc.* **29** 163–73
- Goerke O, Feike E, Heine T, Trampert A and Schubert H 2004 Ceramic coatings processed by spraying of siloxane precursors (polymer-spraying) *J. Eur. Ceram. Soc.* **24** 2141–7
- Colombo P, Paulson T E and Pantano C G 1997 Synthesis of silicon carbide thin films with polycarbosilane (PCS) *J. Am. Ceram. Soc.* **80** 2333–40
- Barroso G, Li Q, Bordia R K and Motz G 2019 Polymeric and ceramic silicon-based coatings—a review *J. Mater. Chem. A* **7** 1936–63
- O'Shaughnessy W S, Gao M L and Gleason K K 2006 Initiated chemical vapor deposition of trivinyltrimethylcyclotrisiloxane for biomaterial coatings *Langmuir* **22** 7021–6
- Zhao J J, Wang M H, Jebutu M S, Zhu M H and Gleason K K 2019 Fundamental nanoscale surface strategies for robustly controlling heterogeneous nucleation of calcium carbonate *J. Mater. Chem. A* **7** 17242–7
- Sojoudi H, McKinley G H and Gleason K K 2015 Linker-free grafting of fluorinated polymeric cross-linked network bilayers for durable reduction of ice adhesion *Mater. Horiz.* **2** 91–99
- O'Shaughnessy W S, Murthy S K, Edell D J and Gleason K K 2007 Stable biopassive insulation synthesized by initiated chemical vapor deposition of poly(1,3,5-trivinyltrimethylcyclotrisiloxane) *Biomacromolecules* **8** 2564–70
- Moon H et al 2015 Synthesis of ultrathin polymer insulating layers by initiated chemical vapour deposition for low-power soft electronics *Nat. Mater.* **14** 628–35
- Moreno-Couranjou M, Loyer F, Gryan P, Boscher N D and Choquet P 2020 Insights into switchable thermoresponsive copolymer layers by atmospheric pressure plasma-initiated chemical vapour deposition *Plasma Process. Polym.* **17** 1900172
- Oh M S, Jeon M, Jeong K, Ryu J and Im S G 2021 Synthesis of a stretchable but superhydrophobic polymer thin film with conformal coverage and optical transparency *Chem. Mater.* **33** 1314–20
- Trujillo N J, Wu Q G and Gleason K K 2010 Ultralow dielectric constant tetravinyltetramethylcyclotetrasiloxane films deposited by initiated chemical vapor deposition (iCVD) *Adv. Funct. Mater.* **20** 607–16
- Nguyen B, Dabir S, Tsotsis T and Gupta M 2019 Fabrication of hydrogen-selective silica membranes via pyrolysis of

- vapor deposited polymer films *Ind. Eng. Chem. Res.* **58** 15190–8
- [31] Malen J A, Baheti K, Tong T, Zhao Y, Hudgings J A and Majumdar A 2011 Optical measurement of thermal conductivity using fiber aligned frequency domain thermorefectance *J. Heat Transfer* **133** 081601
- [32] Ong W-L, O'Brien E S, Dougherty P S M, Paley D W, Fred Higgs C, McGaughey A J H, Malen J A and Roy X 2017 Orientational order controls crystalline and amorphous thermal transport in superatomic crystals *Nat. Mater.* **16** 83–88
- [33] Cahill D G 2004 Analysis of heat flow in layered structures for time-domain thermorefectance *Rev. Sci. Instrum.* **75** 5119–22
- [34] Chen N, Reeja-Jayan B, Liu A D, Lau J, Dunn B and Gleason K K 2016 iCVD cyclic polysiloxane and polysilazane as nanoscale thin-film electrolyte: synthesis and properties *Macromol. Rapid Commun.* **37** 446–52
- [35] Aresta G, Palmans J, van de Sanden M C M and Creatore M 2012 Initiated-chemical vapor deposition of organosilicon layers: monomer adsorption, bulk growth, and process window definition *J. Vac. Sci. Technol. A* **30** 041503
- [36] Grill A and Neumayer D A 2003 Structure of low dielectric constant to extreme low dielectric constant SiCOH films: Fourier transform infrared spectroscopy characterization *J. Appl. Phys.* **94** 6697–707
- [37] Burkey D D and Gleason K K 2004 Organosilicon thin films deposited from cyclic and acyclic precursors using water as an oxidant *J. Electrochem. Soc.* **151** F105
- [38] Coclite A M, Ozaydin-Ince G, Palumbo F, Milella A and Gleason K K 2010 Single-chamber deposition of multilayer barriers by plasma enhanced and initiated chemical vapor deposition of organosilicones *Plasma Process. Polym.* **7** 561–70
- [39] Zhao J J, Wang M H and Gleason K K 2017 Stabilizing the wettability of initiated chemical vapor deposited (iCVD) polydivinylbenzene thin films by thermal annealing *Adv. Mater. Interfaces* **4** 1700270
- [40] Burkey D D and Gleason K K 2003 Structure and mechanical properties of thin films deposited from 1,3,5-trimethyl-1,3,5-trivinylcyclotrisiloxane and water *J. Appl. Phys.* **93** 5143–50
- [41] Oh T and Choi C K 2010 Comparison between SiOC thin film by plasma enhanced chemical vapor deposition and SiO₂ thin film by Fourier transform infrared spectroscopy *J. Korean Phys. Soc.* **56** 1150–5
- [42] Šimon I and McMahon H O 1953 Study of the structure of quartz, cristobalite, and vitreous silica by reflection in infrared *J. Chem. Phys.* **21** 23–30
- [43] O'Hare L-A, Hynes A and Alexander M R 2007 A methodology for curve-fitting of the XPS Si 2p core level from thin siloxane coatings *Surf. Interface Anal.* **39** 926–36
- [44] Roualdes S, Berjoan R and Durand J 2001 ²⁹Si NMR and Si2p XPS correlation in polysiloxane membranes prepared by plasma enhanced chemical vapor deposition *Sep. Purif. Technol.* **25** 391–7
- [45] Thorpe M F 1985 Rigidity percolation *Physics of Disordered Materials* ed D Adler, H Fritzsche and S R Ovshinsky (Boston: Springer) pp 55–61
- [46] Phillips J C 1979 Topology of covalent non-crystalline solids I: short-range order in chalcogenide alloys *J. Non-Cryst. Solids* **34** 153–81
- [47] Thorpe M F 1983 Continuous deformations in random networks *J. Non-Cryst. Solids* **57** 355–70
- [48] Qiu M J, Du W W, Luo X Y, Zhu S Y, Luo Y W and Zhao J J 2022 Vapor-phase molecular doping in covalent organosiloxane network thin films via a Lewis acid–base interaction for enhanced mechanical properties *ACS Appl. Mater. Interfaces* **14** 22719–27
- [49] Kim B J, Seong H, Shim H, Lee Y I and Im S G 2017 Initiated chemical vapor deposition of polymer films at high process temperature for the fabrication of organic/inorganic multilayer thin film encapsulation *Adv. Eng. Mater.* **19** 1600870
- [50] Shen Y L 2019 Nanoindentation for testing material properties *Handbook of Mechanics of Materials* eds C H Hsueh, S Schmauder, C S Chen, K K Chawla, N Chawla, W Q Chen and Y Kagawa (Singapore: Springer) pp 1981–2012
- [51] Döhler G H, Dandoloff R and Bilz H 1980 A topological-dynamical model of amorphycity *J. Non-Cryst. Solids* **42** 87–95
- [52] Ghossoub M G, Lee J-H, Baris O T, Cahill D G and Sinha S 2010 Percolation of thermal conductivity in amorphous fluorocarbons *Phys. Rev. B* **82** 195441
- [53] He H and Thorpe M F 1985 Elastic properties of glasses *Phys. Rev. Lett.* **54** 2107–10
- [54] Wen Q B, Yu Z J and Riedel R 2020 The fate and role of *in situ* formed carbon in polymer-derived ceramics *Prog. Mater. Sci.* **109** 100623
- [55] Schütz A, Günthner M, Motz G, Greißl O and Glatzel U 2012 Characterisation of novel precursor-derived ceramic coatings with glass filler particles on steel substrates *Surf. Coat. Technol.* **207** 319–27
- [56] Feng K, Chen Y, Deng P S, Li Y Y, Zhao H X, Lu F G, Li R F, Huang J and Li Z G 2017 Improved high-temperature hardness and wear resistance of Inconel 625 coatings fabricated by laser cladding *J. Mater. Process. Technol.* **243** 82–91
- [57] Gridi O, Hamidouche Z M, Kermel C and Leriche A 2022 Mechanical and sandblasting erosion resistance characterization of chemical strengthened float glass *Bol. Soc. Esp. Cerám. Vidr.* **61** 229–40
- [58] Fellah M, Labaiz M, Assala O, Iost A and Dekhil L 2013 Tribological behaviour of AISI 316L stainless steel for biomedical applications *Tribol. Mater. Surf. Interfaces* **7** 135–49
- [59] Xu Y B, Wang H T, Tanaka Y, Shimono M and Yamazaki M 2007 Measurement of interfacial thermal resistance by periodic heating and a thermo-reflectance technique *Mater. Trans.* **48** 148–50
- [60] Sandell S, Maire J, Chávez-Ángel E, Sotomayor Torres C M, Kristiansen H, Zhang Z L and He J Y 2020 Enhancement of thermal boundary conductance of metal–polymer system *Nanomaterials* **10** 670
- [61] Jeong M, Freedman J P, Liang H J, Chow C-M, Sokalski V M, Bain J A and Malen J A 2016 Enhancement of thermal conductance at metal-dielectric interfaces using subnanometer metal adhesion layers *Phys. Rev. Appl.* **5** 014009
- [62] Eom J-H, Kim Y-W, Kim K J and Seo W-S 2018 Improved electrical and thermal conductivities of polysiloxane-derived silicon oxycarbide ceramics by barium addition *J. Eur. Ceram. Soc.* **38** 487–93
- [63] Mazo M A, Palencia C, Nistal A, Rubio F, Rubio J and Oteo J L 2012 Dense bulk silicon oxycarbide glasses obtained by spark plasma sintering *J. Eur. Ceram. Soc.* **32** 3369–78
- [64] Gurlo A, Ionescu E, Riedel R, Clarke D R and Green D J 2016 The thermal conductivity of polymer-derived amorphous Si–O–C compounds and nano-composites *J. Am. Ceram. Soc.* **99** 281–5
- [65] Cahill D G, Watson S K and Pohl R O 1992 Lower limit to the thermal conductivity of disordered crystals *Phys. Rev. B* **46** 6131–40

- [66] Agne M T, Hanus R and Snyder G J 2018 Minimum thermal conductivity in the context of *diffuson*-mediated thermal transport *Energy Environ. Sci.* **11** 609–16
- [67] Allen P B and Feldman J L 1993 Thermal conductivity of disordered harmonic solids *Phys. Rev. B* **48** 12581–8
- [68] Aryana K, Stewart D A, Gaskins J T, Nag J, Read J C, Olson D H, Grobis M K and Hopkins P E 2021 Tuning network topology and vibrational mode localization to achieve ultralow thermal conductivity in amorphous chalcogenides *Nat. Commun.* **12** 2817